A. Frye[a,*], R. H. French[a,b], D. A. Bonnell[a]
[a] Department of Materials Science and Engineering, University of Pennsylvania, Philadelphia, PA, USA
[b] DuPont Co. Central Research, Experimental Station, Wilmington, DE, USA
* Presently at IBM Microelectronics

Optical properties and electronic structure of oxidized and reduced single-crystal strontium titanate

Dedicated to Professor Dr. Dr. h. c. Manfred Rühle on the occasion of his 65th birthday

© 2003 Carl Hanser Verlag, Munich, Germany www.hanser.de/mk Not for use in internet or intranet sites. Not for electronic distribution.

The measured optical and transport properties of single-crystal $SrTiO_3$ have been determined as a function of oxidation and reduction using spectroscopic ellipsometry, Hall and resistivity measurements. A decrease in the valence to conduction band transitions across the band gap, from O 2p to Ti 3d states, is observed by decreases in both the index of refraction and the extinction coefficient at the region of the band gap energy, in the ultraviolet region. This supports the model that oxygen nonstoichiometry depletes the O 2p densities of states in the top of the upper valence band, in agreement with previous photoemission studies. The degree of reduction decreases the band gap energy, calculated from the optical absorption coefficient spectra. The direct gap energy varies from 3.88 to 3.58 eV, and the indirect band gap energy ranging from 3.77 to 3.0 eV with increasing reduction. The resistivities of the samples decrease with increased reduction, yet free carrier densities are also found to decrease, suggesting an increase in electron mobility with reduction.

Keywords: $SrTiO_3$; Strontium titanate; Oxidation/reduction; Electronic structure; Optical properties

1. Introduction

Transition metal oxides (TMO) are important technological materials [1–3] and have received much scientific attention in recent years. The properties of strontium titanate have been studied extensively for well over thirty years, and these efforts have produced a coherent picture of some phenomena along with some controversies [4–7]. A thorough understanding of most of these properties requires knowledge of the electronic structure of the bulk material [8] along with its interfaces and surfaces. However, the variability in oxidation state of the transition metal cation largely accounts for the great variation in physical properties of $SrTiO_3$ and the observation of various stable bulk, interface and surface structures. Interfaces in $SrTiO_3$ have been studied extensively with transmission electron microscopy (TEM) [9, 10], and the atomic and electronic structure of interfaces in $SrTiO_3$ has been studied using scanning transmission electron microscopy [11] including the quantitative analysis of valence electron energy-loss spectra [12, 13] to determine the London dispersion forces [14]. The study of the structure of, and processes at, surfaces [15] of $SrTiO_3$ using a wide variety of experimental tools is well-represented in the literature [16].

In addition to its scientific role as the prototypical TMO, strontium titanate has widespread application in technology. It is a good substrate candidate for use in photoelectrochromic devices where a charge transfer (redox) reaction is facilitated by a defect state energetically located in the band gap of the oxide [17]. Similar surface defect-related properties have made $SrTiO_3$ the focus of research in the fields of photocatalysis and solar energy conversion [18, 19]. Advancement in other technologies where $SrTiO_3$ has been identified as a critical or potentially critical material, such as gas sensors [20], superconducting thin film growth [21], and memory storage devices]22], depend on increased understanding of corrosion mechanisms, high-temperature reconstructions, defect interactions, etc., at the surfaces and grain boundaries. Much of the photo- and chemical-reactivity of the (001) surface have been linked to extrinsic states in the forbidden energy [16].

Nominally pure $SrTiO_3$ is an electronic insulator at room temperature. Incorporation of point defects into the lattice can generate free charge carriers or charged ionic species. In the latter case, the defects may be associated or unassociated. In semiconducting $SrTiO_3$ at room temperature the charge carriers are predominately electrons introduced by donor impurity doping or heating in a reducing atmosphere. The latter heat treatment introduces an approximately equivalent density of oxygen vacancies, which are known to exhibit a significantly large lattice mobility, particularly at elevated temperatures [23]. $SrTiO_3$ is thus considered a mixed electronic-ionic conductor.

Recent work [8], using *ab initio* band structure calculations, valence electron energy-loss and vacuum ultraviolet spectroscopies, and spectroscopic ellipsometry, provide an understanding of the bulk electronic structure of oxidized $SrTiO_3$. From this work, the experimentally determined indirect band gap energy is 3.25 eV, while the direct gap energy is 3.75 eV. The conduction bands in $SrTiO_3$ corre-

© 2003 Carl Hanser Verlag, Munich, Germany www.hanser.de/mk Not for use in internet or intranet sites. Not for electronic distribution.

spond to the bands composed of mainly Ti 3d t_{2g} and e_g states, followed at higher energies by the bands of Sr 4d t_{2g} and e_g states, and free electron like states dominating at energies above 15 eV. The upper valence band contains 18 electrons in dominantly O 2p states, hybridized with Ti and Sr states, and has a band width of 5 eV. The interband transitions of the electronic structure of bulk oxidized $SrTiO_3$ at the band gap arise from the O 2p states of the upper valence band going to the Ti 3d bands, and at higher energies to the Sr 4d bands. These transitions span from the indirect band gap energy, of 3.25 up to 15 eV. These will serve as the basis to understand the results presented in the current work.

Here, we use bulk optical and transport measurements to study the changes in the band gap region of single-crystal $SrTiO_3$ as a function of oxidation and reduction, so as to determine changes in the optical properties and the valence and conduction bands of the electronic structure.

2. Experimental

2.1. Sample preparation

Samples were prepared by first orienting a single-crystal boule (obtained from Atomergic Chemetals Corp.) such that the ⟨001⟩ direction was aligned normal to the surface. An observed 4-fold rotational symmetry by back-reflection Laue verified this orientation. The boule was then sliced using a 0.015″ diameter diamond wire blade. The wafers were polished using diamond-impregnated lapping films of grit sizes down to 0.1 μm and finally to 0.05 μm particle size alumina paste.

The crystals were then heat-treated in air with a slow temperature ramp (3 K/min) to 1000 °C, held for 10 h, and subsequently furnace cooled (5 K/min). Platinum electrodes were coated to the samples using Engelhard #6926 unfritted paste, and an initial vacuum heat treatment was used to burn off the paste solvent and form low-resistance contacts [24]. The air-anneal resulted in flat surfaces characterized by plateaus separated by straight-edged (and kinked) multiple unit cell steps, as observed by atomic force microscopy (AFM) measurements (Fig. 1).

The samples were thermally reduced by one of two methods: (1) vacuum annealing by joule heating, or (2) furnace annealing in a hydrogen atmosphere. In the former case, the temperature was monitored by an optical pyrometer.

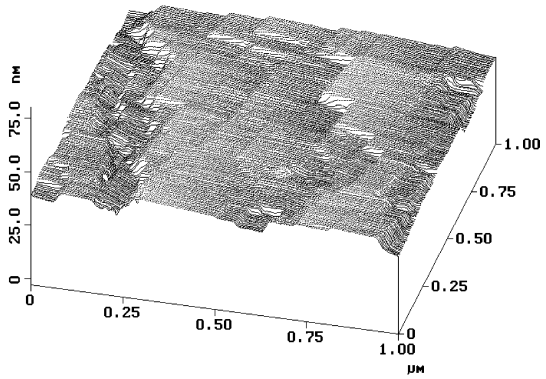

Fig. 1. AFM image showing the stepped surface of $SrTiO_3$ after polishing and air annealing for up to 10 h at 1000 °C.

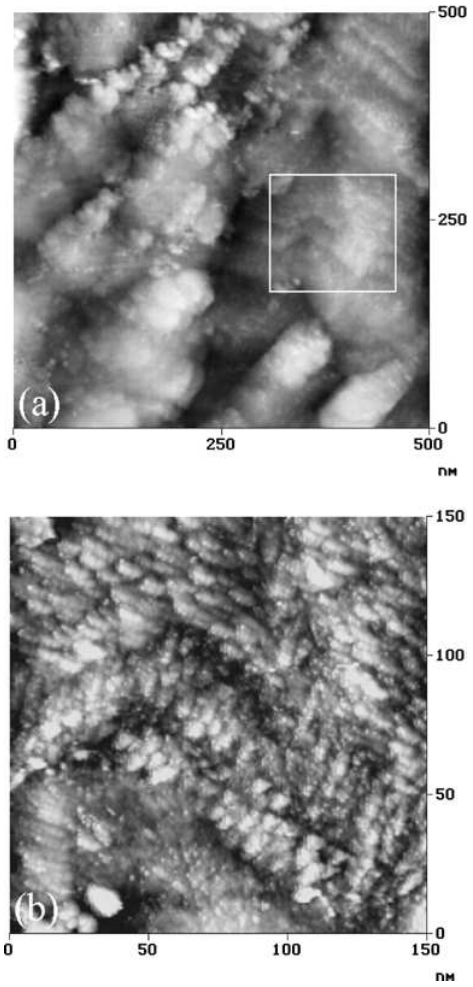

Fig. 2. STM images showing a stepped surface of $SrTiO_3$ after a similar preparation as the sample in Fig. 1 with an additional vacuum anneal at 1000 °C for 30 min. (b) is a magnification of the boxed region appearing in (a).

Upon cooling, the temperature was observed to drop below 800–850 °C (the "freeze-in" point for oxygen vacancies) within 50 to 100 s. The furnace-annealed samples were subsequently air cooled.

After polishing, all samples were etched using a buffered NH_4–HF (BHF) solution for 1.25 min. The pH value was determined to be in the range 4.5–4.7 using colorpHast® indicator strips. This solution is expected to preferentially attack the more basic planes leaving flat surfaces predominately TiO_2-terminated [25]. After the initial vacuum annealing, the samples were briefly re-annealed in air to remove surface carbon contamination and to ensure a common insulating state. Fig. 2 shows the scanning tunneling microscopy (STM) images revealing a stepped surface of $SrTiO_3$ after a similar preparation as the sample in Fig. 1 (i. e., before the BHF etch) with an additional vacuum anneal at 1000 °C for 30 min. Three step stairs could be easily seen in image (a), and the microstructure details around the steps are clearly exhibited in image (b).

Fig. 3 shows an AFM image of a typical sample prepared with the BHF solution before additional vacuum annealing. Fig. 4 shows AFM images of a typical sample similarly prepared after being heavily reduced by vacuum annealing.

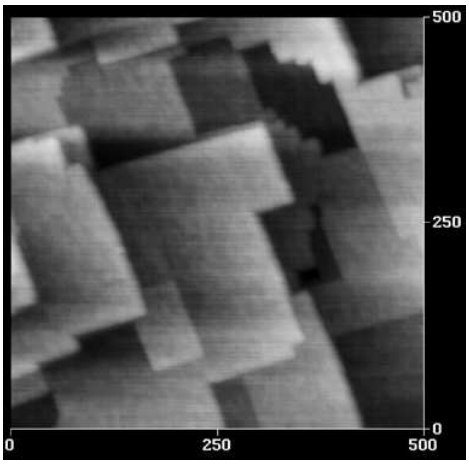

Fig. 3. A 500 nm × 500 nm AFM image showing a stepped surface of $SrTiO_3$ after a similar preparation as the sample in Fig. 1 with an additional BHF etching and re-annealing in air.

Preparing the samples in this way resulted in clean (i. e., carbon-free) surfaces that could be reduced in a controlled manner to obtain samples with varying conductivities and surface morphologies.

2.2. Hall and resistivity measurements

Hall measurements were performed in the standard configuration with the exception that a bipolar power source, modulated at 1 kHz, supplied an alternating current to the sample and a lock-in amplifier was used to detect the Hall voltage. The magnetic field was 9.5 kGauss, and the currents used were between 35 and 85 mA.

2.3. Deep ultraviolet spectroscopic ellipsometry

2.3.1. Data acquisition

Spectroscopic ellipsometry is a technique that yields the optical constants of a material from measurements of polarized reflected light [26–28]. The technique generally consists of illuminating the surface with circularly- or elliptically-polarized monochromated light and detecting changes in amplitude and phase upon reflection. One component of the incident light is linearly polarized in the plane of incidence (the p wave) and another component is linearly polarized normal to the plane of incidence (the s wave). The actual parameters measured by an ellipsometer are the angles Ψ and Δ, where the former is a measure of the ellipticity introduced to the reflected wave due to a relative change in amplitude between the p and s waves, and the latter is a measure of the change in phase difference between the p and s waves upon reflection. The data was acquired and analyzed using a J. A. Woollam DUV-Vase spectroscopic ellipsometer [29].

2.3.2. Optical modeling

Subsequently, an appropriate model must be assumed for the reflecting system upon solving an equation of the form [30]

$$\tan \Psi e^{i\Delta} = \frac{r^{\mathrm{p}}(\hat{n}, \varphi)}{r^{\mathrm{s}}(\hat{n}, \varphi)} \qquad (1)$$

where r^{p} and r^{s} are called the Fresnel reflection coefficients. They are functions of known experimental parameters (such as the angle of incidence, φ, and the refractive index of air) and the (unknown) complex index of refraction, $\hat{n}$, of the material under investigation. The appropriate forms of r^{p} and r^{s} depend on the assumed model of the reflecting system. In the present case, a simple model with two reflecting surfaces (the top and bottom of a single crystal) was sufficient to fit the experimental data. Optical transmission measurements were performed to obtain better accuracy in the optical constants in spectral regions where absorption is very small and thus the ellipsometer produced data with greater error.

2.3.3 Band gap fitting procedure

Band gap values can be fitted to the experimentally determined optical absorption coefficients using established procedures [31]. The ellipsometrically determined extinction coefficient spectra, shown in Fig. 5a, are used to calculate the absorption coefficient (α), which is related to the extinction coefficient by

$$\alpha = \frac{4\pi k}{\lambda} \qquad (2)$$

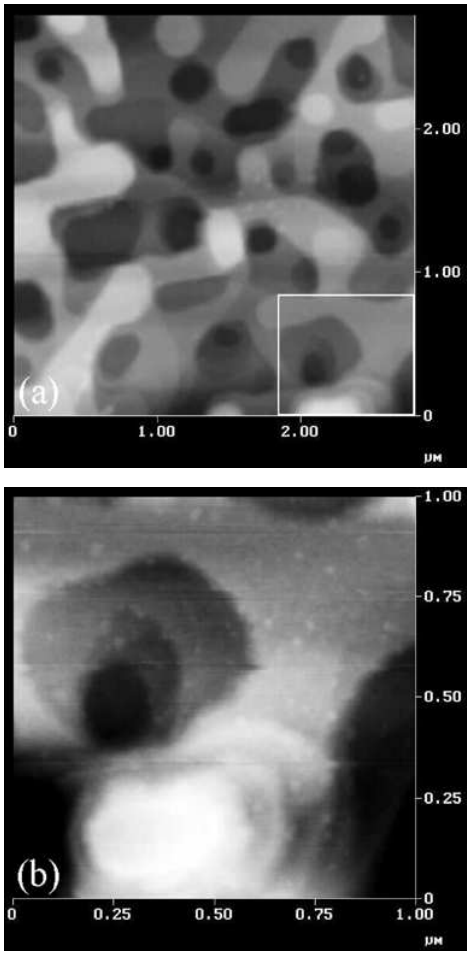

Fig. 4. AFM images of heavily reduced $SrTiO_3$ (001) showing morphological development as compared to the air-annealed sample in Fig. 3. (a) 3 μm × 3 μm scan, (b) 1 μm × 1 μm scan of lower right edge of the image (a).

© 2003 Carl Hanser Verlag, Munich, Germany www.hanser.de/mk Not for use in internet or intranet sites. Not for electronic distribution.

where λ is the wavelength of the light. The optical absorption coefficient results, in units of 1/cm, are shown in Fig. 6a. Within the independent electron approximation, the absorption coefficient near the fundamental absorption edge is assumed to be approximated by [32]

$$\alpha \sim \frac{\left(h\omega - E_g\right)^m}{h\omega} \tag{3}$$

where $h\omega = E_{ph}$ is the energy of the incident photon, and the value of m depends on the transition mechanism. For indirect transitions $m = 2$; for direct transitions $m = 0.5$. Fitting $\left(\alpha E_{ph}\right)^{\frac{1}{m}}$ versus E_{ph} near the absorption edge obtains a linear fit when the appropriate transition mechanism is assumed, and the intercept with the abscissa gives the energy of the transition.

3. Results and discussion

3.1. Hall and resistivity measurements of oxidized and reduced single-crystal $SrTiO_3$

Hall and resistivity measurements are summarized in Table 1, and the results for the hydrogen-reduced samples (the H series) are shown in Fig. 7. These samples show a decrease in resistivity with increasing annealing temperature. The measured carrier density, however, apparently also decreases with reduction temperature as shown in Fig. 7.

From the semi-classical theory for electron dynamics, the carrier density is simply related to the Hall coefficient (R_H) and can be written in terms of measurable parameters as

$$n_c = \frac{IH_z}{V_H et} \tag{4}$$

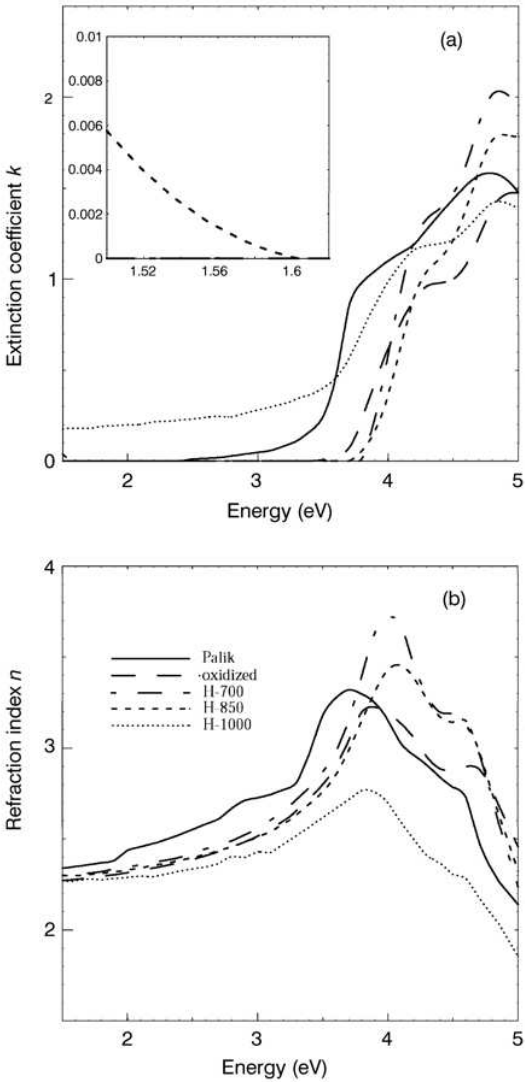

Fig. 5. The dispersion curves for the optical constants k (a) and n (b) of $SrTiO_3$. The extinction coefficient (a) and index of refraction (b) are shown for oxidized and reduced single crystals, as indicated by the legend. These are also compared to literature values measured over the same spectral range (solid curve). The inset in (a) shows an absorption tail for H–850 near the "red" region of the visible spectrum.

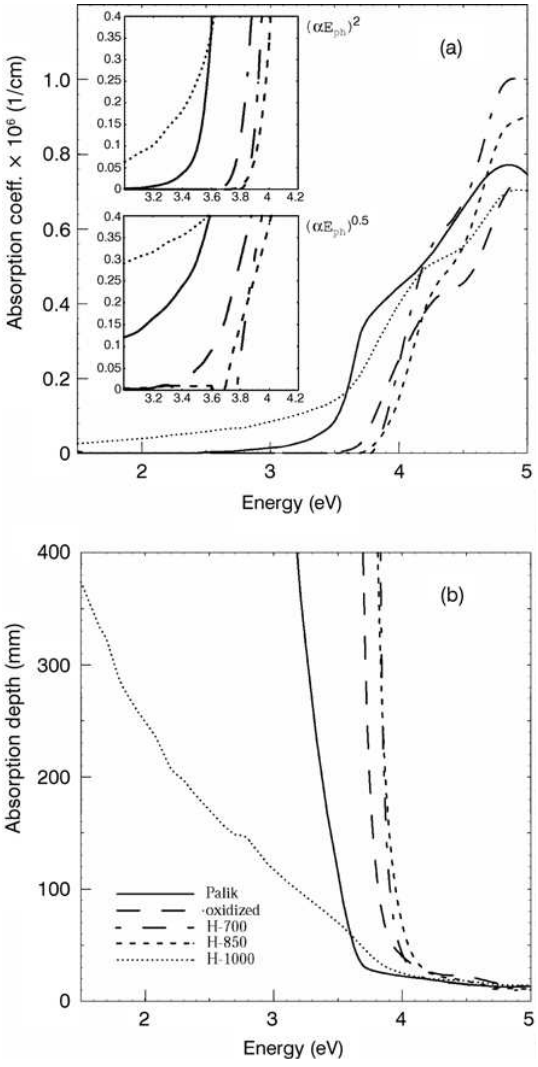

Fig. 6. (a) The dispersion curves for the absorption coefficient of $SrTiO_3$. The insets demonstrate that this measurement gives evidence of both direct and indirect transition mechanisms. The transition energies are deduced by linear fitting near the absorption edge. (b) The inverse of the curves in (a).

© 2003 Carl Hanser Verlag, Munich, Germany www.hanser.de/mk Not for use in internet or intranet sites. Not for electronic distribution.

Table 1. Thermal history of the oxidized samples, and Hall and resistivity measurements.

Sample ID	Thermal history	V_H (mV)	ρ (Ωcm)	$n_c \times 10^{+17}$ (cm^{-3})
V–930	930 °C, 10 min/vacuum	–	–	–
V–1100	1100 °C, 12 min/vacuum	–	–	–
V–930Nb	930 °C, 10 min/vacuum	2.1	0.042 ± 0.001	8.8
H–700	700 °C, 2 h/H_2 furnace	2.0	0.430 ± 0.008	3.3 ± 0.7
H–850	850 °C, 2 h/H_2 furnace	2.4	0.069 ± 0.002	3.2 ± 1.1
H–1000	1000 °C, 2 h/H_2 furnace	3.2	0.026 ± 0.003	1.3 ± 0.5

where I is the measured current, t is the thickness of the sample, V_H is the Hall voltage and H_z is the applied magnetic field. Furthermore, for n-type extrinsic materials, the Hall mobility, μ_H, is given by

$$\mu_H = \frac{R_H}{\rho} = \frac{1}{en\rho} \tag{5}$$

which is very nearly equivalent to the true carrier drift mobility when acoustic phonon scattering is the predominant scattering mechanism [33]. It is well known, however, that electron–lattice coupling in transition metal oxides (i. e., polar crystals) can lead to small or large polaron formation. These mechanisms may introduce uncertainty in mobility measurements obtained by the Hall method.

Sample V-930Nb in Table 1 was intentionally Nb-doped to 2000 at.ppm, or approximately 10^{19} cm^{-3}. Using Eq. (5) and assuming this carrier density gives a mobility of 3.73 cm^2/Vs, whereas the measured carrier density gives 168.34 cm^2/Vs. The former estimate is close to tabulated values for "small" x in $SrTiO_{3-x}$ [34]. The latter value, however, sounds reasonable and is still an order of magnitude less than the electron mobilities in semiconducting Si (1500 cm^2/Vs), Ge (3900 cm^2/Vs), or GaAs (8500 cm^2/Vs). The reported purity of this sample was 10 at.ppm (i. e., an accidental impurity density of 10^{17} cm^{-3}). Therefore, accidental acceptor impurity compensation for the donor impurities does not appear to be an acceptable explanation for the two orders of magnitude discrepancy in n. It is possible that the sample was unintentionally underdoped or that a negligible fraction of the Nb reactivated following the post oxidation thermal treatment as described in Table 1.

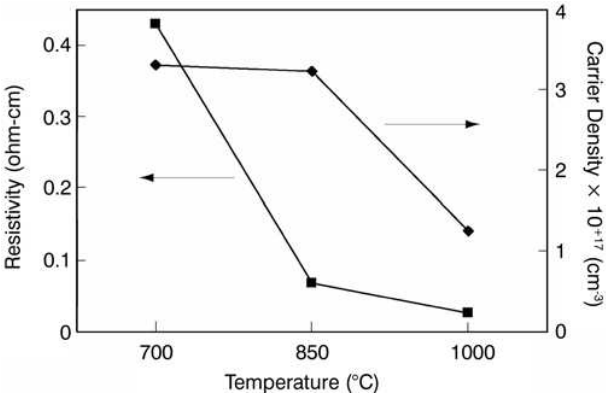

Fig. 7. Resistivity and carrier density of undoped single-crystal $SrTiO_3$ as a function of annealing temperature.

3.2. Deep ultraviolet spectroscopic ellipsometry

All samples appeared spatially uniform in color. Sample H–700 appeared transparent and colorless, H–850 transmitted in the blue region of the visible spectrum, and H–1000 appeared black. All samples can be expected to strongly absorb light with energies above approximately the 3.25 eV band gap energy where electronic interband transitions are excited between the highest occupied valence bands and the lowest unoccupied conduction bands. The changing color of the crystals with increasing defect density suggests increases in optical absorption at energies throughout the infrared and visible regions of the spectrum. This interpretation is confirmed by the optical measurements presented below.

3.3. Optical constants and fitted band gap energies

Fig. 5 shows the measured dispersion of the extinction coefficient (k) and the refractive index (n) for each sample in the H series. Also included are measurement results of an oxidized sample as well as the tabulated values for nominally undoped $SrTiO_3$ at room temperature, taken from Palik [35]. The results of the oxidized crystal are comparable to Palik's literature compilation, but the transition energies found here exhibit a shift to higher energies. The cause of this spectral shift is unclear, it may arise due to differences in prior thermal treatments and relative changes in the oxidation or reduction of the $SrTiO_3$ crystals studied. All curves in Fig. 5b show normal dispersion, an increase in refractive index with increasing photon energy, up to some energy where n reaches a maximum. At energies above 3.8 eV to 4.1 eV, n decreases with increasing photon energy, commonly referred to as the region of anomalous dispersion. A shoulder appears above the peak energy for all samples. This is indicative of two overlapping dissipation processes.

The allowed direct transitions in cubic $SrTiO_3$ were determined by Casella [36] to be: $\Gamma_{15} \rightarrow \Gamma_{25'}$; $\Delta_5 \rightarrow \Delta_{2'}$; $\Delta_5 \rightarrow \Delta_5$; $X_{5'} \rightarrow X_3$; $X_{4'} \rightarrow X_5$; and $X_{5'} \rightarrow X_5$. Based on the observed splitting (0.86 eV) of the primary absorption peak from reflectivity data, however, Cardona [37] concluded that both $X_{4'} \rightarrow X_5$ and $X_{5'} \rightarrow X_5$ transitions accounted for the observed dispersion in the refractive index. A similar splitting of 0.8 eV is observed at the onset of anomalous dispersion for the oxidized curve in Fig. 5b. The decreasing intensity in both n and k among the H series in this spectral region can thus be interpreted as a decrease in the optical joint density of states for these transitions. It has been established that this is caused by a decrease in the density of states of the upper valence band upon reduction [38].

© 2003 Carl Hanser Verlag, Munich, Germany www.hanser.de/mk Not for use in internet or intranet sites. Not for electronic distribution.

© 2003 Carl Hanser Verlag, Munich, Germany www.hanser.de/mk Not for use in internet or intranet sites. Not for electronic distribution.

Table 2. Band gap energies fitted from Figs. 5 and 6.

Sample ID	Direct gap energy (eV)	Indirect gap energy (eV)
Palik	3.52	3.28
Oxidized	3.79	3.59
H–700	3.88	3.77
H–850	3.90	3.68
H–1000	3.58	3.00

Direct and indirect band gap energies have been fitted to the optical absorption coefficient in Fig. 6a and are summarized in Table 2. Direct band gap energies are found to be ranging from 3.58 to 3.90 eV and indirect band gap energies from 3.00 to 3.77 eV as a function of oxidation/reduction. The band gaps reported here for the oxidized crystal are comparable to those of van Benthem et. al. [13] who reported direct and indirect band gap energies of 3.75 and 3.25 eV, respectively. In comparison, band gap energies fitted to Palik's literature compilation for oxidized $SrTiO_3$ give direct and indirect band gap energies of 3.52 and 3.28 eV, respectively, consistent with the shift to lower energies of Palik's reported optical constants.

3.4. Effects of oxidation and reduction on the properties of $SrTiO_3$

There is an apparent increase in the optical joint density of states for interband transitions within the early stages of reduction. The high-frequency dielectric function $\hat{\varepsilon} = n^2 - k^2$ is expected to decrease with increasing direct band gap if the dispersion can be approximated as the response of a single harmonic, or Lorentz, oscillator [39]. Fig. 8, which plots the dielectric function below the anomalous dispersion region, shows that this behavior is observed only between the H–700 and H–850 samples. Moreover, the observed decrease in the dielectric function ($\hat{\varepsilon}$) from 1.6 to 2.6 eV with decreasing band gap from H–850 to H–1000 is a consequence of the fact that a single Lorentz oscillator is not a reasonable model for optical absorption in heavily reduced $SrTiO_3$. A more complex behavior is observed.

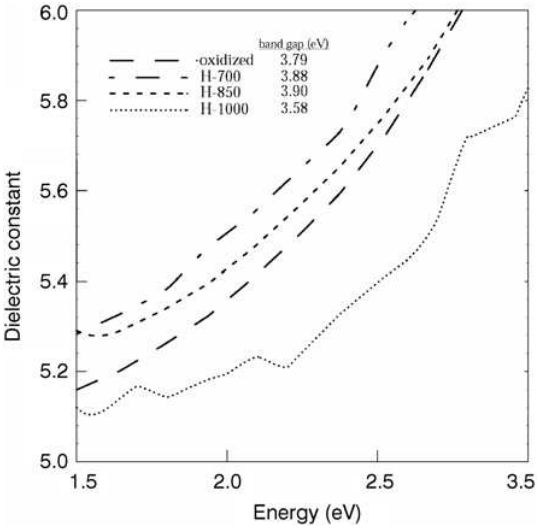

Fig. 8. Dielectric function $\hat{\varepsilon} = n^2 - k^2$ of $SrTiO_3$ below anomalous dispersion.

The properties of nonstoichiometric crystals are regularly interpreted in terms of a random distribution of point defects. From a thermodynamic point of view, however, if the enthalpy of formation of associated defects (i. e., oxygen vacancy pairs) is large and negative, then the free energy of the crystal will be minimized by the formation of defect clusters. Recent theoretical work suggests that oxygen vacancy clustering is required in order to form localized states in the band gap of $SrTiO_3$ [40]. Such states will have the potential to depopulate the conduction band by free carrier trapping. It is reasonable to expect that defect clustering plays a role in crystals with larger nonstoichiometry. It should be emphasized, however, that a high overall defect density is neither a necessary nor sufficient condition for the formation of band gap states. Rather than a random distribution, it may be more appropriate to think in terms of a statistical distribution of point defects, where local defect cluster densities may vary. The static, or low-frequency, dielectric constant tends to decrease with increasing nonstoichiometry [41] such that if the defect state energies are assumed to be approximated by the hydrogenic model [42], then a distribution of binding energies will accompany a distribution of defect densities. This can lead to optical absorption over a broad spectral range in the visible (assuming defect to conduction band transitions are symmetry allowed), as observed in Fig. 6b.

The above interpretation implies that as vacancy density increases to the point where association could occur the number of mobile charge carriers could decrease. Hence, a decrease in free carrier density, as measured by a Hall probe, would be expected. This was indeed observed, as shown in Fig. 7. The values for n in Table 1 are within the range observed in previous studies on reduced single-crystal $SrTiO_3$ [43, 44]. The predicted Hall mobilities for H–700, H–850, and H–1000 are 44, 281, and 1,945 $cm^2/V\,s$, respectively. On the other hand, the average value obtained by previous authors is 6.07 $cm^2/V\,s$ [44]. If the carrier mobility is assumed to be independent of carrier density and oxygen vacancy clustering, and given by the latter value, one can work backwards using sample resistivities in Table 1 to predict the carrier densities to be 2.45, 0.24, 1.5, and $3.96 \times 10^{19}\,cm^{-3}$, for V–930Nb, H–700, H–850, and H–1000, respectively. With this assumption, the carrier density for the doped crystal agrees better with the estimated value based on the doping specification.

4. Conclusions

The measured optical and transport properties of single-crystal $SrTiO_3$ have been determined as a function of oxidation and reduction, using spectroscopic ellipsometry and Hall and resistivity measurements. A decrease in the valence-to-conduction band transitions across the band gap, from O 2p to Ti 3d states, is observed by decreases in both the index of refraction and the extinction coefficient at the region of the band gap energy, in the ultraviolet region. This supports the model that oxygen nonstoichiometry depletes the O 2p densities of states in the top of the upper valence band, in agreement with previous photoemission studies. The degree of reduction decreases the band gap energy cal-

culated from the optical absorption coefficient spectra, with the direct gap energy varying from 3.88 to 3.58 eV and the indirect band gap energy ranging from 3.77 to 3.0 eV with increasing reduction. The resistivities of the samples decrease with increased reduction, yet free carrier densities are also found to decrease, suggesting an increase in electron mobility with reduction.

The authors would like to acknowledge M. F. Lemon for technical assistance with ellipsometry measurements and the comments and assistance of G. L. Tan with the manuscript. This work was partially supported under Department of Energy Office of Basic Energy Science DE-FG02-00ER45813, under National Science Foundation Award DMR-0010062 in cooperation with European Union Contract G5RD-CT-2001-00586, and facilities use was supported by NSF MRSEC.

References

[1] T.K. Gupta: J. Am. Ceram. Soc. 73, 1817 (1990).
[2] D.A. Crandles, B. Nicholas, C. Dreher, C.C. Homes, A.W. McConnell, B.P. Clayman, W.H. Gong, J.F. Greedan: Phys. Rev. B 59, 12842 (1999).
[3] M. Leonhardt, J. Jamnik, J. Maier: Electrochem. & Solid State Lett. 2, 333 (1999).
[4] N. Bickel, G. Schmidt, K. Heinz, K. Müller: Phys. Rev. Lett. 62 2009 (1989).
[5] T. Hikita, T. Hanada, M. Kudo, M. Kawai: Surface Science, 287, 377 (1993).
[6] U. Balachandran, N.G. Eror: J. Mat. Sci. 17, 2133 (1982).
[7] S. Witek, D.M. Smyth, H. Pickup: J. Am. Ceram. Soc. 67, 372 (1984).
[8] K. van Benthem, C. Elsässer, R.H. French: J. Appl. Phys. 90, 6156 (2001).
[9] N.D. Browning, J.P. Buban, H.O. Moltaji, S.J. Pennycook, G. Duscher, U.D. Johnson, P.R. Rodrigues, V.P. Dravid: Appl. Phys. Lett. 74, 2638 (1999).
[10] F. Ernst, O. Kienzle, M. Rühle: J. Eur. Ceram. Soc. 19, 665 (1999).
[11] V. Ravikumar, R.P. Rodrigues, V.P. Dravid: J. Phys. D: Appl. Phys. 29, 1799 (1996).
[12] A.D. Dorneich, R.H. French, H. Müllejans, S. Loughin, M. Rühle: J. Microscopy, 191, 286 (1998).
[13] K. van Benthem, R.H. French, W. Sigle C. Elsässer, M. Rühle: Ultramicroscopy 86, 303 (2001).
[14] R.H. French: J. Am. Ceram. Soc. 83, 2117 (2000).
[15] D.P. Woodruff, T.A. Delchar: Modern Techniques of Surface Science, Cambridge University Press, Cambridge (1994).
[16] V.E. Henrich, P.A. Cox: The Surface Science of Metal Oxides, Cambridge University Press, Cambridge (1994).
[17] J.P. Ziegler, E.K. Lesniewski, J.C. Hemminger: J. Appl. Phys. 61, 3099 (1987); J.P. Ziegler, J.C. Hemminger, J. Electrochem. Soc. 134, 358 (1987).
[18] N.B. Brookes, F.M. Quinn, G. Thornton: Physica Scripta 36, 711 (1987).
[19] P. Salvador, C. Gutiérrez, G. Campet, P. Hagenmüller: J. Electrochem. Soc. 131, 550 (1984).
[20] E.B. Várhegyi, I.V. Perczel, J. Gerblinger, M. Fleischer, H. Meixner, J. Giber: Sensors and Actuators B 18–19, 569 (1994).
[21] D.M. Hill, H.M. Meyer III, J.H. Weaver: J. Appl. Phys. 65, 4943 (1989).
[22] M. Copel, P.R. Duncomber, D.A. Neumayer, T.M. Shaw, R.M. Tromp: Appl. Phys. Lett. 70, 3227 (1997).
[23] J. Blanc, D.L. Staebler: Phys. Rev. B 4 , 3548 (1971).
[24] A. Frye: Ph. D. Thesis, University of Pennsylvania, Philadelphia, PA (1999).
[25] M. Kawasaki, K. Takahashi, T. Maeda, R. Tsuchiya, M. Shinohara, O. Ishiyama, T. Yonezawa, M. Yoshimoto, H. Koinuma: Science 266, 1540 (1994).
[26] J.A. Woollam, B. Johs, C.M. Herzinger, J. Hilfiker, R. Synowicki, C.L. Bungay: SPIE, CR 72, 3 (1999).
[27] B. Johs, R.H. French, F.D. Kalk, W.A. McGahan, J.A. Woollam: Optical Interference Coatings, SPIE 2253, 1098 (1994).
[28] B. Johs, J.A. Woollam, C.M. Herzinger, J. Hilfiker, R. Synowicki, C.L. Bungay: SPIE, CR 72, 29 (1999).
[29] J.A. Woollam Co., Inc., 645 M Street, Suite 102, Lincoln, NE 68508 USA, http://www.jawoollam.com/.
[30] H.G. Tompkins: A User's Guide to Ellipsometry, Academic Press, Boston, MA (1993).
[31] R.H. French, R. Abou-Rahme, D.J. Jones, L.E. McNeil: Ceramic Trans. 28, 63 (1992).
[32] S.M. Sze: Physics of Semiconductor Devices, John Wiley & Sons, New York (1981).
[33] J.P. McKelvey: Solid State and Semiconductor Physics, Krieger Pub. Co. (1982).
[34] P.A. Cox: Transition Metal Oxides: An Introduction to Their Electronic Structure and Properties, Oxford University Press, New York (1992).
[35] E.D. Palik (Ed.): Handbook of Optical Constants of Solids II, Academic Press, San Diego, CA (1991).
[36] R.C. Casella: Phys. Rev. 154, 743 (1967).
[37] M. Cardona: Phys. Rev. 140, A 651 (1965).
[38] V.E. Henrich, G. Dresselhaus, H.J. Zeiger: Phys. Rev. B 17, 4908 (1978).
[39] F. Wooten: Optical Properties of Solids, Academic Press, San Diego, CA (1972).
[40] N. Shanthi, D.D. Sarma: Phys. Rev. B 57, 2153 (1998).
[41] H.B. Lal: Indian J. Pure Appl. Phys. 8, 81 (1970).
[42] P.A. Cox: Transition Metal Oxides: An Introduction to Their Electronic Structure and Properties, Oxford University Press, New York (1992).
[43] W.S. Baer: Phys. Rev. 144, 734 (1966).
[44] H. Yamada, G.R. Miller: J. Solid State Chem. 6, 169 (1973).

(Received October 15, 2002)

Correspondence address

Dr. R. H. French
DuPont Central Research
E 356–384, Exp. Sta., Wilmington, DE 19880–0356, USA
Tel.: +1 302 695 1319
Fax: +1 302 695 1664
E-mail: Roger.H.French@USA.dupont.com

© 2003 Carl Hanser Verlag, Munich, Germany www.hanser.de/mk Not for use in internet or intranet sites. Not for electronic distribution.